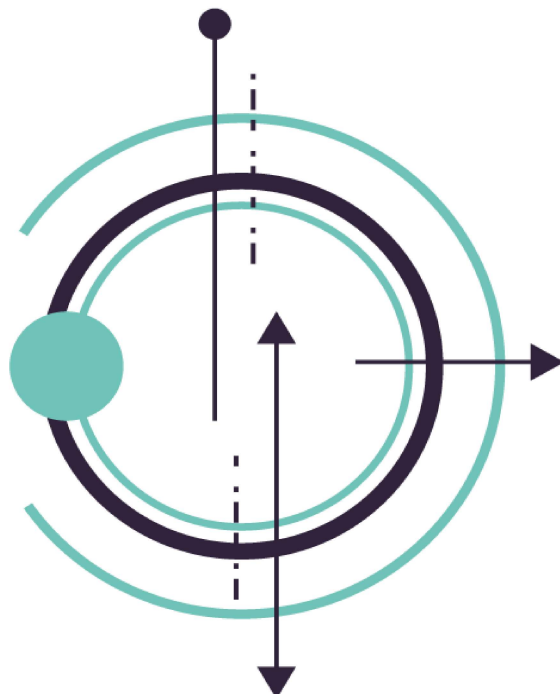


IMVIP 2022



Conference Proceedings

24th Irish Machine Vision and Image Processing Conference

31st August – 2nd September, Queen's University, Belfast

Sponsored by:



FACULTY OF
ENGINEERING
AND PHYSICAL
SCIENCES



Published by the Irish Pattern Recognition & Classification Society

iprcs.org

ISBN 978-0-9934207-7-1

©2022

This work is distributed free of charge by the Irish Pattern Recognition & Classification Society on behalf of the Irish Machine Vision & Image Processing Conference, and the contributing authors to this conference. Both organisers and authors own the rights of their contribution to this book.

Geometrically reconstructing confocal microscopy images for modelling the retinal microvasculature as a 3D cylindrical network

Evan P. Troendle^{1,*}, Peter Barabas¹, and Tim M. Curtis¹

¹Wellcome-Wolfson Institute for Experimental Medicine, Queen's University Belfast, Belfast, BT9 7BL, Northern Ireland, United Kingdom

*Corresponding author: Evan P. Troendle, E.Troendle@qub.ac.uk

Abstract

Microvascular networks can be modelled as a network of connected cylinders. Presently, however, there are limited approaches with which to recover these networks from biomedical images. We have therefore developed and implemented computer algorithms to geometrically reconstruct three-dimensional (3D) retinal microvascular networks from micrometre-scale imagery, resulting in a concise representation of two endpoints and radius for each cylinder detected within a delimited text file. This format is suitable for a variety of purposes, including efficient simulations of molecular delivery. Here, we detail a semi-automated pipeline consisting of the detection of retinal microvascular volumes within 3D imaging datasets, the enhancement and analysis of these volumes for reconstruction, and the geometric construction algorithm itself, which converts voxel data into representative 3D cylindrical objects.

Keywords: Image Processing, Retina, Vasculature, 3D Reconstruction, Shape Recovery

1 Introduction

Measuring three-dimensional (3D) blood vessel volumes is an essential step in analysing healthy capillary network architectures as well as deviations from them during pathological processes. From the clinical perspective, quantitative analysis of blood vessel topography in 3D offers a baseline to compare against and provides a basis for understanding blood flow dynamics or communication between blood vessel and tissue volumes [Secomb, 2008]. Further, reconstruction of complex, realistic vascular networks allows for efficient computer simulations that physically model the transport of molecules from the vasculature into tissues [Troendle et al., 2018]. Efficient representations of 3D vascular structures are paramount to identify the structural features that impact extravasation and molecular delivery within heterogeneous microvasculatures to advance systemic drug delivery and development strategies.

Retinal microvasculatures are valuable to investigate scientifically as they are readily accessible, yet highly dense and complex microvascular systems that can be adequately imaged in full at high resolution *ex vivo* [Prahst et al., 2020]. The study of retinal microvascular complications in most mammals can be used to better understand disease progression in humans [Curtis et al., 2009] as their anatomical features and physiology recapitulate many features found within human retinas [Chang, 2013]. At present, therapeutics for advanced retinal vascular diseases are primarily administered intravitreally [Virgili et al., 2018, Solomon et al., 2019]. However, a better understanding of systemic pharmaceutical delivery to the retina could assist in the development of less-invasive drug delivery approaches.

In this study, we describe a sequence of semi-automated image processing techniques that can be used to geometrically reconstruct the retinal microvasculature in 3D as a network of connected cylinders. These techniques allow for further 3D quantification of the retinal microvasculature to better understand and model retinal diseases and therapies. Furthermore, this methodology should be applicable to the study of any microvascular bed.

2 Methods

2.1 Preparing the retina for microscopy

Due to biological and technical limitations at present, it is only feasible to experimentally acquire microvascular imagery in sufficient resolution for 3D reconstruction *ex vivo*. Present *in vivo* techniques are of insufficient resolution to image the entire retinal microvasculature at the capillary level [Roorda et al., 2006, Yu et al., 2015]. For this study, retinal tissue was harvested from the left eye of a streptozotocin (STZ)-induced diabetic male C57BI6J mouse model aged 19 weeks. STZ was dissolved in 0.1M citrate buffer pH 4.5 at 10 mg/ml and injected intraperitoneally once per day on five consecutive days at a dose of 50 mg STZ / kg body weight. The eye was fixed for 1 hour in 4% paraformaldehyde solution and stored in phosphate-buffered saline (PBS) until immunohistochemistry was performed to prepare the blood vessels for acquisition using confocal scanning laser microscopy.

For detecting blood vessels, biotinylated isolectin B4 from the plant *Griffonia simplicifolia* was used, as it specifically binds to the α -galactose residues of glycoproteins, which are typically present on endothelial cells [Kirkeby and Moe, 2001]. While the lectin serves as the primary agent for recognizing the target molecules, the secondary in this case was streptavidin conjugated to the fluorophore Alexa FluorTM 568. The murine retina was permeabilised using a solution of TritonX-100 [Johnson, 2013] in PBS[T8787-100ML, Merck] (0.5% v/v), followed by incubation with isolectin B4 [L2140-1MG, Merck] (1:200) in PBS+TritonX-100 for 4 days at 4 °C on a rocker. Subsequently, PBS was used to wash the retinal samples, using a fast PBS wash (10 exchanges) followed by another wash with 30 minute incubation in refreshed PBS on rocker at 4 °C over ten washing iterations; the total washing time amounted to 6.5 hrs. Streptavidin, Alexa FluorTM 568 conjugate [S11226, Thermo Fisher Scientific] (1:200) in PBS+TritonX-100 was incubated overnight at 4 °C on a rocker, followed by the same wash steps that were used after the primary step. Finally, the retina was flat-mounted under dim red light in VECTASHIELD H-1000 [H-1000, Vector Laboratories] and protected under a coverslip.

Animal work was approved by the Queen's University of Belfast Animal Welfare and Ethical Review Body (AWERB). Work adhered to Department of Health, Social Services and Public Safety (DHSSPS) project license PPL2814.

2.2 Scanning confocal microscopy for the acquisition of the retina

A Leica TCS SP8 laser scanning confocal inverted microscopy system [Leica Microsystems] equipped with a 20 \times air objective [Leica 20x HC PL APO CS2; NA = 0.75] was used to image the murine retinal sample from the vitreal surface through the inner retina. The confocal pinhole was set to 1 Airy unit, the scanning speed was 400 Hz, and 512 \times 512 pixels (px.) were captured in each imaging frame across a field of 8 \times 9 laser patterning tiles encompassing the entire flat-mount preparation. The z-step was set to 1 μ m with 75 steps in total, resulting in a tissue depth of 75 μ m; the duration of the image acquisition took 2 hours.

Within the LasX Leica software, x - y images belonging to the same optical plane were stitched with 10% overlap for all z -slices, resulting in aggregated images that best depicted independent focal planes. This yielded a dataset of 75 3890 \times 4343 px. images, with each pixel corresponding to voxels of spatial extent 1.14 μ m \times 1.14 μ m \times 986.6 nm. Image data were exported to an uncompressed 3D Tag Image File Format (TIFF) for input into subsequent processing steps for 3D geometric reconstruction. The maximum intensity z -axis projection of the acquired murine flat-mounted retina is shown in Figure 1.

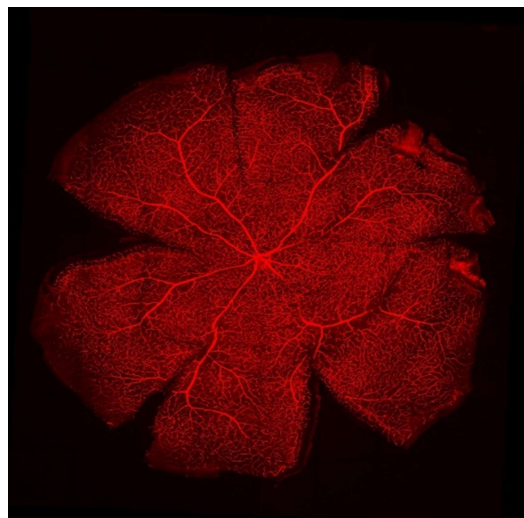


Figure 1: Maximum intensity z -axis projection of the murine flat-mounted retina.

3 Results

3.1 Semi-automated detection and refinement of microvascular volumes in 3D

For the remainder of this study, image processing algorithms utilised the OpenCV C++ API [Bradski, 2000]. To detect microvascular endothelia from the confocal microscopy images, noise was firstly reduced by applying a 2D median filter [Huang et al., 1979] (5×5 px. kernel) over each image slice. Next, a Laplacian of Gaussian [Lindeberg, 2015] filter ($\sigma = 2.0$ px ≈ 2.28 μm) was utilised to further reduce noise and detect edge-like features corresponding to the endothelial boundaries. Following this step, a global intensity threshold was applied to detect the endothelial edges as a binary (i.e., bi-partite-valued) mask.

As the isolectin B4 staining is selective to visualising endothelia, the vessel lumens emitted low to non-detectable fluorescence levels and were not initially included in the binary mask following the application of the global intensity threshold. To recover these regions as part of the total microvascular volume, a filling approach was necessary. Traditional recursive [Newman and Sproull, 1979] or iterative scan-line-based [Vučković et al., 2019] region filling algorithms in 2D and 3D were not suitable for these experimentally-derived images due to the presence of small gaps in the endothelial boundaries that persisted after enhancement (see Figure 2). This necessitated the development of a novel region-filling approach as described below.

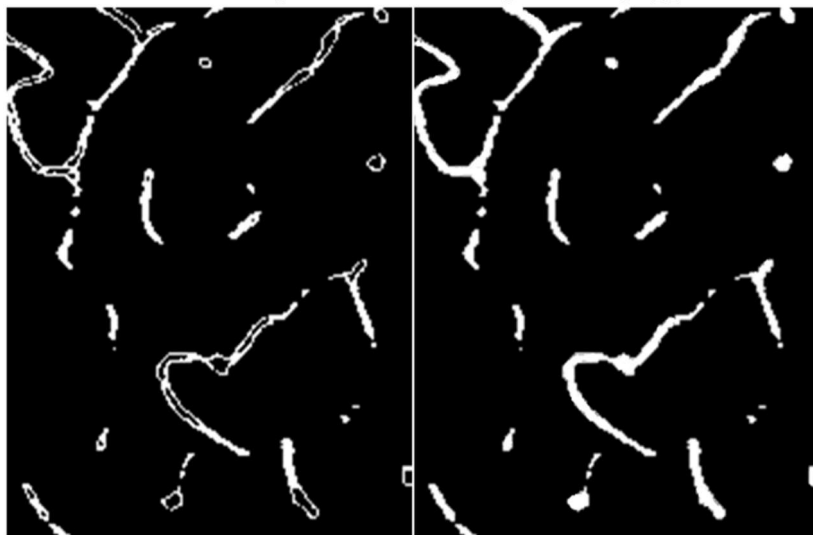


Figure 2: Detection and filling of microvascular volumes from their endothelial boundaries. Left: Boundary pixels of the microvascular endothelia were detected for a subset of the 3D imaging data; note the existence of many small gaps precluding conventional region filling techniques. Right: The resultant data after filling according to the algorithm described in this manuscript.

To fill the microvascular volumes, first-order x -, y -, and z - image intensity (I) partial derivatives (i.e., $\partial I / \partial x$, $\partial I / \partial y$, and $\partial I / \partial z$) were initially assessed for every pixel in the original microscopy data (Figure 1). For each boundary coordinate in the binary mask (Figure 2), an orthogonal unit vector was constructed from the image intensity derivative components. Then, a potential linear filling operation propagated from each boundary coordinate in the direction of the orthogonal vector and was accepted should the voxel march [Amanatides and Woo, 1987] hit another boundary pixel with an orthogonal vector pointing in approximately the opposite direction (e.g., $<5^\circ$ from parallel). This approach can be implemented in 2D as well as 3D, by applying the algorithm within each 2D slice and thus omitting the z - components, resulting in a filled binary microvascular volume.

Following filling, the 3D Euclidean distance transform [Felzenszwalb and Huttenlocher, 2012] and non-maximum suppression [Marin et al., 2015] was applied on the microvascular volume to estimate the vessel centrelines and radii. A depiction of the 3D Euclidean distance transform applied to the microvascular volume as detected and filled by the 2D region filling algorithm is shown in Figure 3.

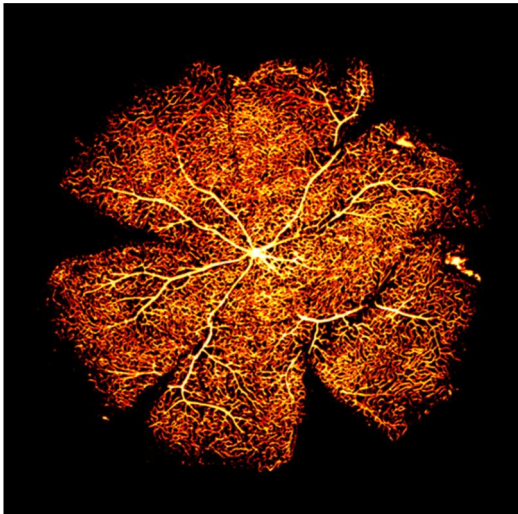


Figure 3: Maximum intensity z -axis projection of the 3D Euclidean distance transform applied to the detected and filled microvascular voxels within the murine flat-mounted retina. Vessel diameters detected ranged from 1.14 to 42.18 μm .

3.2 3D reconstructions of the microvasculature

3.2.1 Surface reconstructions

From the binary mask of the filled microvascular volumes (e.g., Figure 2), a surface mesh of the microvasculature was prepared using isosurface reconstruction via marching cubes [Lorensen and Cline, 1987]. The 3D surface reconstruction of the murine retinal flat-mount is shown in Figure 4.

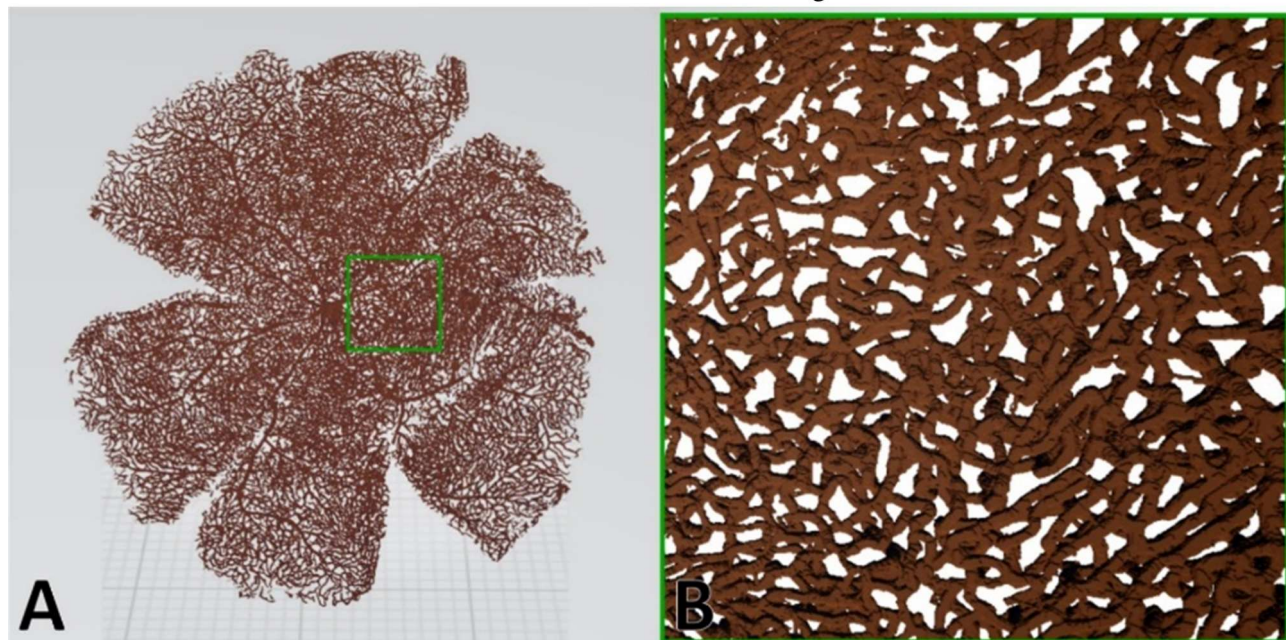


Figure 4: 3D surface mesh of the entire murine retinal flat-mount. A: Isosurface reconstruction of the full binarised imaging dataset allows the representation of microvascular surfaces. B: A zoomed-in region reveals intricate interwoven retinal microvascular layers present in 3D.

3.2.2 Geometric reconstructions

As geometric reconstructions are a computationally expensive task, the application of the algorithm was restricted to a quarter of the retinal flat-mount. To geometrically encode the retinal microvasculature as a series of interconnected cylinders, spherical objects were first detected by marching a series of voxelised spheres in

descending size about the binary mask of voxels detected in the microvasculature, accepting a candidate sphere as present should $\geq 90\%$ of its volume intersect the mask. Regions within the mask occupied by successfully placed spheres were then excluded from the search space until no further potential candidates could be found. The smallest spheres detected ($R = 1 \text{ px. } \approx 1.14 \mu\text{m}$) were omitted from further processing as smaller objects were more likely to represent false-positive detections due to remaining noise as determined by expert inspection. The result of this approach is reflected in Figure 5.



Figure 5: Sphere detection applied to a quadrant of the murine retinal flat-mount. Left: Mean intensity projection denoting spherical detection; Right: The corresponding sphere detection as visualised in 3D.

Next, all possible cylinders were assigned by marching [Amanatides and Woo, 1987] between the centres of all pairs of spheres, tagging a candidate cylinder should a straight 3D line be contained entirely within the detected microvascular volume binary voxel mask. The radius of each cylinder was set to the mean of the two sphere radii. The result of this approach is shown in Figure 6.

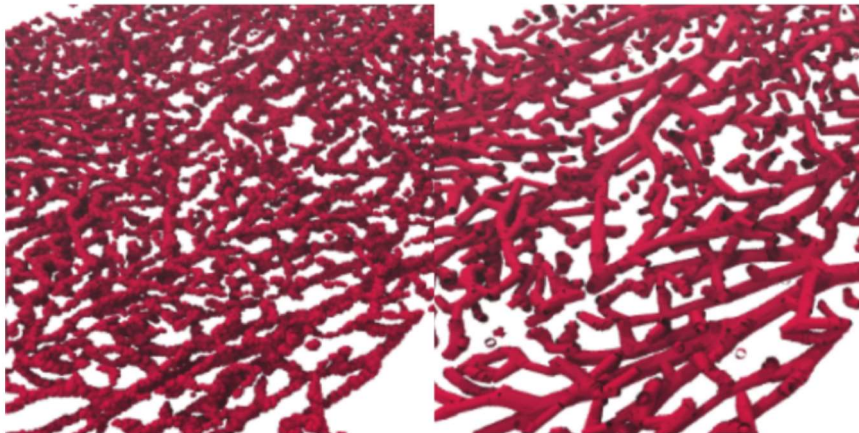


Figure 6: Cylindrification after sphere detection via pairwise marching between spherical nodes constrained within the binary voxel mask. Left: A region of spheres as detected in Figure 5. Right: The resulting cylindrical network following pairwise marching between spherical nodes constrained to the binary voxel mask.

As cylinders are over-detected from the pairwise node marching approach, firstly, trivial cylinders that provide no additional information (i.e., those which are fully contained within others) are removed entirely using rapid point in cylinder detection calculations [Barbier and Galin, 2004]. Next, remaining pairs of cylinders that overlap partially [Ketchel and Larochelle, 2005] are each divided into three cylinders (i.e., pre-overlap, overlap, and post-overlap, relative to each pair) until no colliding cylinders remain apart from end-to-end connections.

Branch points must then be resolved through splitting cylinders at the point of bifurcation according to the centreline detection derived from the distance transform, maintaining appropriate connectivity. Lastly, relatively collinear cylinders that touch end-to-end may be consolidated into lengthier cylinders by evaluating the scalar product of the cylindrical axes to further simplify the vascular network. The memory to store the 3D geometric reconstruction of the retinal microvascular network quadrant as described, which was initially composed of ~209 million 1 byte voxels of input imaging data, is now represented by $N = 98,389$ cylinders, which are each represented by 7 32-bit floating point numbers in the form of two endpoint x -, y -, and z - coordinates with radius or diameter. This corresponds to a reduction in computer memory utilisation by a factor of ~100×.

4 Discussion

The primary purpose for undertaking this work was to retrieve microvasculatures from experimental imagery as input for particle-based simulations of molecular transport [Troendle et al., 2018]. The work presented in this paper provides the necessary platform to perform such simulations within real microvascular networks in the near future. Computer simulations of therapeutic compounds moving within the retinal microvasculature are likely to provide new insights into molecular transport within the retina and avenues for developing improved drug delivery approaches. Additionally, retinal microvascular surface meshes (see Figure 4) may be refined [Garland and Heckbert, 1997] and used for computational fluid dynamics studies [Lu et al., 2016] or as a basis for the development of mimetic *in vitro* microfluidic platforms as derived from retinal imagery.

This study provides a new approach for extracting and cylindrifying microvascular networks from biomedical imagery. Kelch et al. analysed the 3D microvascular topography of a murine lymph node by combining confocal microscopy with image processing [Kelch et al., 2015]. Similar to this study, they developed an alternative algorithm to fill incomplete microvascular volumes. Their goal was to obtain detailed topographic spatial analyses of their microvasculature in 3D, but they did not test the utility of their algorithms for geometric reconstructions. Another protocol for the 3D reconstruction of microvascular networks was recently released by Wächli et al., which utilises corrosion casting, scanning electron microscopy, synchrotron radiation and desktop microcomputed tomography (μ CT) imaging, and computational network analysis [Wächli et al., 2021]. While this work could also be adapted to output 3D cylindrical network models, it does not in its presently published form. Nonetheless, a prevailing limitation within this application area is that the specific image processing parameters and steps needed to perform microvascular geometric reconstructions are dependent upon the features of the biological sample, its preparation for imaging, and the image acquisition modality itself.

The algorithms used in this study for microvascular refinement and geometric detection may facilitate the development of machine learning algorithms to improve predictions of disease risk. For example, the algorithm by Cheung et al. can detect increased probability of cardiac arrests via assessing retinal vessel diameters [Cheung et al., 2021]. Topographic information extracted from 3D cylindrical network models may be used to enhance their predictions. Further, supervised machine learning algorithms can be developed to accelerate the recovery of 3D cylindrical objects from vascular imagery by employing the methods used here to generate labelled target data for training machine learning models.

As medical imaging technology further advances, it may be possible to apply these methods to high resolution 3D *in vivo* microvascular datasets. With the recent development of adaptive optics ocular coherence tomography angiography (AO-OCTA) [Camino et al., 2020], the reconstruction of the human retinal microvasculature may soon be possible *in vivo*.

5 Conclusions

This manuscript describes semi-automated image processing algorithms to geometrically reconstruct the retinal microvasculature in 3D as represented by a network of interconnected cylinders. This work can be further extended by improving computational efficiency of the reconstruction protocols and by assessing the accuracy of this method systematically across a wider array of retinal samples.

Acknowledgments

We would like to thank Northern Ireland Health and Social Care R&D Division (STL/4748/13), and the Medical Research Council (MC_PC_15026) for supporting this research.

Author contributions

EPT & TMC conceived the study. PB conducted the animal research, prepared the retina, and acquired the input imagery. EPT designed and performed the image processing and 3D geometric reconstruction algorithms. EPT drafted the manuscript and produced the graphical figures. EPT, PB, & TMC critically evaluated the manuscript.

References

- [Amanatides and Woo, 1987] Amanatides, J. and Woo, A. (1987). A fast voxel traversal algorithm for ray tracing. In *EG1987 Proceedings (Technical Papers)*.
- [Barbier and Galin, 2004] Barbier, A. and Galin, E. (2004). Fast distance computation between a point and cylinders, cones, line-swept spheres and cone-spheres. *Journal of Graphics Tools*, 9:11–19.
- [Bradski, 2000] Bradski, G. (2000). The OpenCV Library. *Dr. Dobb's Journal of Software Tools*.
- [Camino et al., 2020] Camino, A., Zang, P., Athwal, A., Ni, S., Jia, Y., Huang, D., and Jian, Y. (2020). Sensorless adaptive-optics optical coherence tomographic angiography. *Biomed Opt Express*, 11(7):3952–3967.
- [Chang, 2013] Chang, B. (2013). Mouse models for studies of retinal degeneration and diseases. *Methods in molecular biology (Clifton, N.J.)*, 935:27–39.
- [Cheung et al., 2021] Cheung, C. Y., Xu, D., Cheng, C.-Y., Sabanayagam, C., Tham, Y.-C., Yu, M., Rim, T. H., Chai, C. Y., Gopinath, B., Mitchell, P., Poulton, R., Moffitt, T. E., Caspi, A., Yam, J. C., Tham, C. C., Jonas, J. B., Wang, Y. X., Song, S. J., Burrell, L. M., Farouque, O., Li, L. J., Tan, G., Ting, D. S. W., Hsu, W., Lee, M. L., and Wong, T. Y. (2021). A deep-learning system for the assessment of cardiovascular disease risk via the measurement of retinal-vessel calibre. *Nature Biomedical Engineering*, 5(6):498–508.
- [Curtis et al., 2009] Curtis, T. M., Gardiner, T. A., and Stitt, A. W. (2009). Microvascular lesions of diabetic retinopathy: clues towards understanding pathogenesis? *Eye*, 23(7):1496–1508.
- [Felzenszwalb and Huttenlocher, 2012] Felzenszwalb, P. F. and Huttenlocher, D. P. (2012). Distance transforms of sampled functions. *Theory of Computing*, 8(1):415–428.
- [Garland and Heckbert, 1997] Garland, M. and Heckbert, P. S. (1997). Surface simplification using quadric error metrics. In *SIGGRAPH 1997*, page 209–216. Association for Computing Machinery, Inc.
- [Huang et al., 1979] Huang, T., Yang, G., and Tang, G. (1979). A fast two-dimensional median filtering algorithm. *IEEE Transactions on Acoustics, Speech, and Signal Processing*, 27(1):13–18.
- [Johnson, 2013] Johnson, M. (2013). Detergents: Triton x-100, tween-20, and more. *Materials and Methods*, 3:163.
- [Kelch et al., 2015] Kelch, I. D., Bogle, G., Sands, G. B., Phillips, A. R. J., LeGrice, I. J., and Rod Dunbar, P. (2015). Organ-wide 3d-imaging and topological analysis of the continuous microvascular network in a murine lymph node. *Scientific Reports*, 5(1):16534.
- [Ketchel and Larochelle, 2005] Ketchel, J. S. and Larochelle, P. M. (2005). Collision detection of cylindrical rigid bodies using line geometry. In *Proceedings of IDETC/CIE 2005*, pages 811–825. ASME.

- [Kirkeby and Moe, 2001] Kirkeby, S. and Moe, D. (2001). Binding of Griffonia simplicifolia 1 isolectin B4 (GS1 B4) to α -galactose antigens. *Immunology & Cell Biology*, 79(2):121–127.
- [Lindeberg, 2015] Lindeberg, T. (2015). Image matching using generalized scale-space interest points. *Journal of Mathematical Imaging and Vision*, 52(1):3–36.
- [Lorensen and Cline, 1987] Lorensen, W. E. and Cline, H. E. (1987). Marching cubes: A high resolution 3d surface construction algorithm. In *Proceedings of the 14th Annual Conference on Computer Graphics and Interactive Techniques, SIGGRAPH 1987*, pages 163–169. Association for Computing Machinery, Inc.
- [Lu et al., 2016] Lu, Y., Bernabeu, M. O., Lammer, J., Cai, C. C., Jones, M. L., Franco, C. A., Aiello, L. P., and Sun, J. K. (2016). Computational fluid dynamics assisted characterization of parafoveal hemodynamics in normal and diabetic eyes using adaptive optics scanning laser ophthalmoscopy. *Biomedical Optics Express*, 7(12):4958–4973.
- [Marin et al., 2015] Marin, D., Zhong, Y., Drangova, M., and Boykov, Y. (2015). Thin structure estimation with curvature regularization. In *2015 IEEE International Conference on Computer Vision (ICCV)*, pages 397–405.
- [Newman and Sproull, 1979] Newman, W. M. and Sproull, R. F. (1979). *Interactive Raster Graphics: Filling Areas*, book section 17, page 253. McGraw-Hill, Inc., 2nd edition.
- [Prahst et al., 2020] Prahst, C., Ashrafzadeh, P., Mead, T., Figueiredo, A., Chang, K., Richardson, D., Venkataraman, L., Richards, M., Russo, A. M., Harrington, K., Ouarne, M., Pena, A., Chen, D. F., Claesson-Welsh, L., Cho, K. S., Franco, C., and Bentley, K. (2020). Mouse retinal cell behaviour in space and time using light sheet fluorescence microscopy. *eLife*, 9.
- [Roorda et al., 2006] Roorda, A., Garcia, C. A., Martin, J. A., Poonja, S., Queener, H., Romero-Borja, F., Sepulveda, R., Venkateswaran, K., and Zhang, Y. (2006). What can adaptive optics do for a scanning laser ophthalmoscope? *Bulletin of the Belgian Society of Ophthalmology*, (302):231–44.
- [Secomb, 2008] Secomb, T. W. (2008). Theoretical models for regulation of blood flow. *Microcirculation*, 15(8):765–775.
- [Solomon et al., 2019] Solomon, S. D., Lindsley, K., Vedula, S. S., Krzystolik, M. G., and Hawkins, B. S. (2019). Anti-vascular endothelial growth factor for neovascular age-related macular degeneration. *Cochrane Database of Systematic Reviews*, (8).
- [Troendle et al., 2018] Troendle, E. P., Khan, A., Searson, P. C., and Ulmschneider, M. B. (2018). Predicting drug delivery efficiency into tumor tissues through molecular simulation of transport in complex vascular networks. *Journal of Controlled Release*, 292:221–234.
- [Virgili et al., 2018] Virgili, G., Parravano, M., Menchini, F., and Evans, J. R. (2018). Anti-vascular endothelial growth factor for diabetic macular oedema. *Cochrane Database of Systematic Reviews*, (10).
- [Vučković et al., 2019] Vučković, V., Arizanović, B., and Le Blond, S. (2019). Generalized n-way iterative scanline fill algorithm for real-time applications. *Journal of Real-Time Image Processing*, 16(6):2213–2231.
- [Wälchli et al., 2021] Wälchli, T., Bisschop, J., Miettinen, A., Ulmann-Schuler, A., Hintermüller, C., Meyer, E. P., Krucker, T., Wälchli, R., Monnier, P. P., Carmeliet, P., Vogel, J., and Stampanoni, M. (2021). Hierarchical imaging and computational analysis of three-dimensional vascular network architecture in the entire postnatal and adult mouse brain. *Nature Protocols*, 16(10):4564–4610.
- [Yu et al., 2015] Yu, P. K., Balaratnasingam, C., Xu, J., Morgan, W. H., Mammo, Z., Han, S., Mackenzie, P., Merkur, A., Kirker, A., Albiani, D., Sarunic, M. V., and Yu, D.-Y. (2015). Label-free density measurements of radial peripapillary capillaries in the human retina. *PLOS ONE*, 10(8):e0135151.